PNAS RESEARCH ARTICLE | CHEMISTRY

# Pressure aging: An effective process to liberate the power of high-pressure materials research

Hui Luo[a,1], Hongli Xuan[a,1], Dong Wang[a], Ziwan Du[b], Zhongyang Li[a], Kejun Bu[a], Songhao Guo[a], Yuhong Mao[a], Fujun Lan[a], Fuyang Liu[a], Yanfeng Yin[c], Wenming Tian[c], Qingyang Hu[a], Gang Liu[a,d], Haozhe Liu[a], Qiaoshi Zeng[a,d], Yang Ding[a], Yongping Fu[e], Qian Li[b], Shengye Jin[c], Wenge Yang[a], Ho-Kwang Mao[a,d,2], and Xujie Lü[a,2]

Affiliations are included on p. 6.

Contributed by Ho-kwang Mao; received August 19, 2024; accepted November 15, 2024; reviewed by Mario Santoro and Zhongwu Wang

**High pressure can create extreme conditions that enable the formation of novel materials and the discovery of new phenomena. However, the ability to preserve the desirable characteristics of materials obtained under high pressure has remained an elusive challenge, as the pressure-induced changes are typically reversible, except for the pressure-induced chemical reactions such as polymerization of hydrocarbons. Here, we propose the concept of "pressure aging" (PA) that enables the permanent locking-in of high-pressure structures and their associated enhanced properties in functional materials. Specifically, through the application of PA at 3.3 GPa for 24 h, the two-dimensional ferroelectric $CuInP_2S_6$ exhibits a permanent change in Cu configuration after the pressure is fully released. This leads to a 2.5-fold enhancement in remanent polarization and an increase in $T_c$ from 317 K to 583 K. In contrast, the samples underwent a compression–decompression cycle but without PA showed only reversible changes in their characteristics. We elucidate the relaxation dynamics during PA using the Kohlrausch–Williams–Watts function, providing valuable insights into the temporal evolution of both structural and property changes. Furthermore, the broad applicability of PA strategy has been validated across different materials, underscoring its versatility. Notably, the pressures involved are industrially attainable, and the sample sizes are scalable. Consequently, the implementation of this impactful PA approach introduces a groundbreaking unique dimension to high-pressure research, with significant potential across various scientific domains.**

high pressure | aging | permanent preservation | property enhancement | relaxation dynamics

## Significance

A key challenge in the field of high-pressure research has been the preservation of the desirable characteristics of materials achieved under high pressure, as the unique structures and enhanced properties tend to revert to their original states once the pressure is released. Here, we propose the concept of "pressure aging" (PA) to address this long-standing challenge. This approach enables the permanent locking-in of high-pressure structures and the associated enhanced properties in functional materials. Notably, this PA concept is broadly applicable across a wide range of materials with different structural characteristics, and the pressures required are industrially attainable, facilitating the seamless translation of this approach into potential applications.

Pressure, as a thermodynamic variable, could profoundly alter all states of matter (1–4). High-pressure research has shown a significant impact on a wide range of communities from earth sciences to physics and further to materials science and chemistry, where numerous new phenomena and principles are established and novel structures and materials are formed (5–14). A key challenge in high-pressure research lies in preserving the desirable characteristics of materials achieved under high pressure, as the unique structures and enhanced properties tend to revert to their original states once the pressure is released (15–21). This reversible nature of pressure-enabled modifications significantly limits the practical applications of these otherwise remarkable materials.

Based on different time scales, the high-pressure research can be generally divided into three regimes (22–24). Static compression generated by diamond anvil cell (DAC) or large volume press lays in the range from seconds to hours; shock compression applies high pressure to materials in the range from microseconds to nanoseconds; the intermediate time regime, between microsecond to second, can be accessed with rapid pressure loading using a pneumatic diaphragm (gas membrane) or a piezoelectric actuator. All these approaches center around the pressure loading process. Up till now, the impact of the duration spent at the desired pressures, that is "aging," has long been overlooked. This temporal aspect of high-pressure research remains an unexplored field with significant potential for new discoveries.

Aging or ripening has long been appreciated in food industry, which brings flavorful foods like wine and cheese (Fig. 1*A*) (25, 26). Such a process involves a gradual change or transformation over time that improves the quality of the item being aged in specific environments. Here, we surprisingly find that the aging process shows remarkable impacts on the structures and physical properties of diverse materials under high pressures (Fig. 1*B*), resulting in permanent structural changes and highly favorable performance outcomes. In particular, the van der Waals (vdW) $CuInP_2S_6$, known as one of the most promising two-dimensional (2D) ferroelectric materials (27), exhibits a significant improvement in

Author contributions: H.L., H.X., H.-K.M., and X.L. designed research; H.L., H.X., Z.L., F.L., and X.L. performed research; D.W., Z.D., F.L., Q.H., H.L., Q.Z., Y.D., and W.Y. contributed new reagents/analytic tools; H.L., H.X., D.W., K.B., S.G., Y.M., Y.Y., W.T., G.L., Y.F., Q.L., S.J., and X.L. analyzed data; Z.L. carried out ferroelectric measurements; F.L. prepared the sample using a large volume press; and H.L., H.X., H.-K.M., and X.L. wrote the paper.

Reviewers: M.S., Istituto Nazionale di Ottica (CNR-INO); and Z.W., Cornell University.

The authors declare no competing interest.



[1]H.L. and H.X. contributed equally to this work.

[2]To whom correspondence may be addressed. Email: maohk@hpstar.ac.cn or xujie.lu@hpstar.ac.cn.

This article contains supporting information online at https://www.pnas.org/lookup/suppl/doi:10.1073/pnas.2416835121/-/DCSupplemental.

Published December 12, 2024.

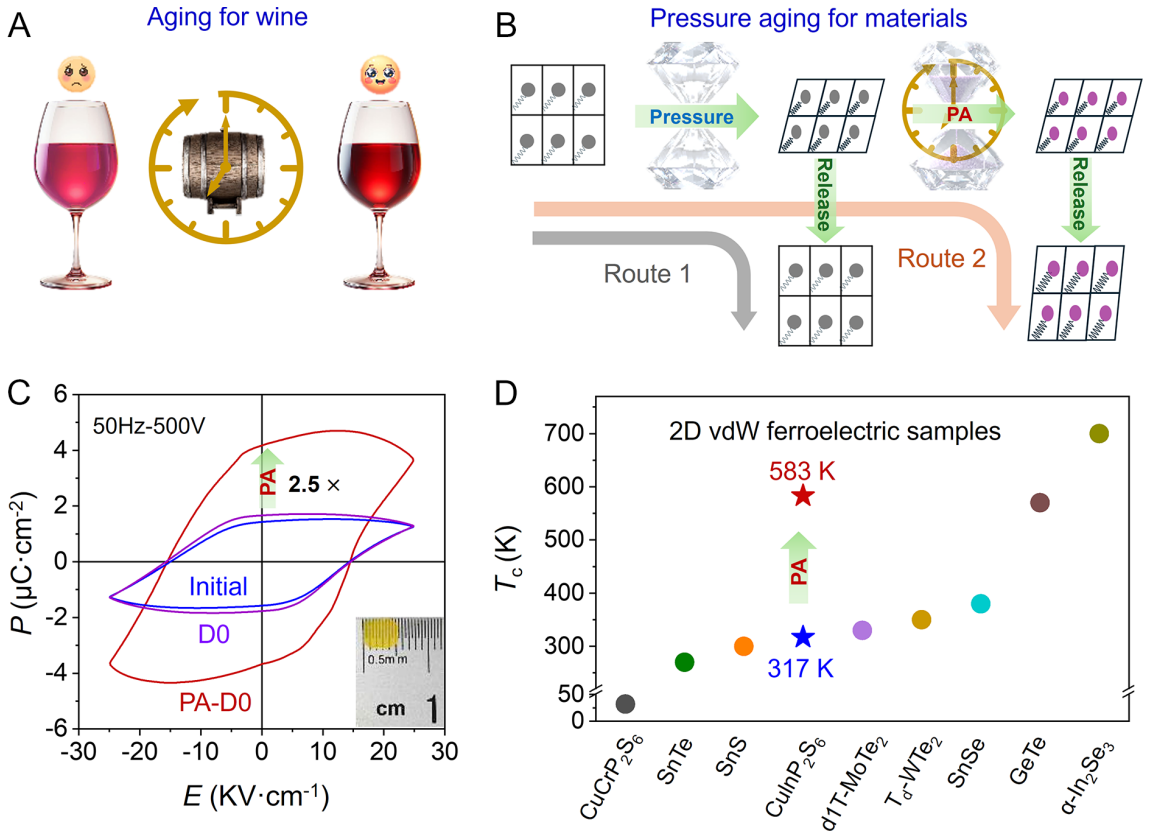


**Fig. 1.** The concept of pressure aging (PA) and its impacts on materials such as $CuInP_2S_6$. (*A*) Aging or ripening process used in food industry like wine. (*B*) Illustration of PA strategy for materials that exhibits remarkable impact on the structures. (*C*) 2.5-fold enhancement in the remanent polarization of ferroelectric $CuInP_2S_6$ after the PA treatment, whereas the sample without PA shows negligible change. Inset displays an image of the $CuInP_2S_6$ crystal subjected to PA treatment using a large volume press. (*D*) 266 K increase of Tc from 317 K to 583 K for $CuInP_2S_6$ and the comparison with other 2D ferroelectric materials.

its ferroelectric properties through PA treatment at 3.3 GPa for a duration of 24 h. As a result, the remanent polarization increased by 2.5 times and the Curie temperature ($T_c$) raised by 266 K even after the pressure was fully released. Importantly, this concept is applicable to a broad class of materials, and the pressures required are industrially attainable. The scalability of sample sizes enables the seamless translation of this approach to larger-scale applications. This transformative PA strategy marks a significant milestone of high-pressure research, paving the way for the rational engineering of functional materials with enhanced and durable performance characteristics.

## Results and Discussion

**Proof of Concept of PA for $CuInP_2S_6$.** As a proof of concept, we first applied the PA strategy to treat the ferroelectric van der Waals (vdW) material $CuInP_2S_6$, yielding a permanent change in cationic configuration of the material along with a significant improvement in its ferroelectric and nonlinear optical (NLO) properties. In the experimental setup, a piece of $CuInP_2S_6$ crystal was loaded into a DAC and gradually compressed to 3.3 GPa. After reaching the desired pressure, the sample was subjected to an aging period of 24 h before decompression to ambient pressure. For comparison, a control experiment was conducted using another piece of $CuInP_2S_6$ from the same crystal, which underwent the same compression–decompression procedure (typically lasting less than 30 min) but without the aging step. Intriguingly, the remanent polarization ($P_r$) of $CuInP_2S_6$ underwent PA treatment increased by about 2.5 times compared with which at initial conditions (Fig. 1*C* and *SI Appendix*, Figs. S1–S3). While the crystal treated by pressure but without PA process shows a negligible change of the ferroelectric property. Meanwhile, the $T_c$ of $CuInP_2S_6$ has experienced a substantial increase after the PA treatment, boosting from 317 K to an impressive 583 K (Fig. 1*D* and *SI Appendix*, Fig. S4). Importantly, such a pressure is industrially available, and the sample as large as 6 millimeters has been obtained using a large volume press (inset of Fig. 1*C*).

Given the challenges and unreliability associated with in situ measurements of ferroelectric properties, we monitor the in situ evolution of second-harmonic generation (SHG) to more effectively elucidate the structure–property relationship. As displayed in Fig. 2*A* and *SI Appendix*, Fig. S5, the regular pressure-treating process (without aging) shows reversible variation of SHG. Specifically, the SHG intensity of $CuInP_2S_6$ increases with pressure increasing, which is enhanced by 12 times at 3.3 GPa compared to its initial value. During the decompression process, the SHG intensity follows a similar trend and returns to a value that is close to the initial one. However, as shown in Fig. 2*B* and *SI Appendix*, Fig. S6, the pressure-induced enhancement of 12 times in SHG can be maintained after pressure releasing for the sample underwent PA process for a duration of 24 h. This indicates that the dynamics associated with high-pressure aging and release-pressure quenching are distinct, enabling the preservation of the desirable characteristics achieved under high pressure. Consequently, the structural changes induced by pressure can be preserved following aging even after the pressure is fully released, which contribute to the improved SHG property. Interestingly, during the PA process at 3.3 GPa, the SHG intensity exhibits a continuous increase and eventually reaches a plateau over a period of 12 h, as shown in Fig. 2*C*. This observation indicates a prolonged "reaction" occurring under high pressure that requires a relatively extended period of time, which will be elaborated on later.

From a structural perspective, $CuInP_2S_6$ possesses a 2D layered structure with Cc noncentrosymmetry at ambient conditions. Within each layer, there is a sulfur framework featuring octahedral cages that are partially filled by indium (In) and P – P units, as depicted in Fig. 2*D*. The initial positions of Cu cations can be divided into two categories (28, 29): displaced upward ($Cu^u$) and downward ($Cu^d$) from the middle of the layer (octahedron centers) and the proportions of $Cu^u$ and $Cu^d$ are 0.9 and 0.1, respectively. It has been reported that the Cu position plays a significant role in influencing the ferroelectric and NLO properties (30–33). Through single-crystal X-ray diffraction (XRD) analysis (*SI Appendix*, Fig. S7 and Table S1), it is revealed that the Cu position in $CuInP_2S_6$ crystal exhibits negligible change upon pressure release when the sample is subjected to the compression-decompression cycle but without the PA process, as shown in the middle panel of Fig. 2*E*. In contrast, for the sample that underwent the PA treatment, both the Cu position and the $Cu^u/Cu^d$ ratio exhibit obvious changes after the pressure is released to ambient conditions (right panel of Fig. 2*E*). Further analysis reveals that the dispersion of Cu cations distribution becomes more dispersive along a polar axis and more polarized after PA treatment, in comparison to the initial state (*SI Appendix*, Tables S2–S4 and Fig. S8). Such permanent structural modification induced by the PA treatment is pivotal, as it demonstrates the ability of PA to induce lasting changes in the atomic-scale arrangement of materials. Consequently, the PA-induced permanent alteration in the Cu configuration enhances the structural polarization within the $CuInP_2S_6$ crystal and thus contributes to the observed enhancement in SHG performance (31, 32, 34). Note that the improved SHG property of the $CuInP_2S_6$ crystal underwent PA treatment exhibits a negligible change over six months and showcases the thermal stability up to 200 °C (*SI Appendix*, Fig. S9).

To gain deeper insights into the pressure-induced variations of local structures, in situ Raman spectra of $CuInP_2S_6$ were collected during high-pressure treatments, both with and without the PA process. In Fig. 3*A* and *SI Appendix*, Fig. S10, the $P_1$ and $P_3$ modes are identified as the out-of-plane vibration of Cu and the asymmetric stretching vibration of Cu–S (35), respectively, which are highly sensitive to the Cu position. During compression, the weakening of the $P_1$ intensity confirms the increase in dispersion of Cu cations. Comparing the Raman spectra in Fig. 3 *B* and *C*, it can be observed that the $P_1$ mode exhibits an irreversible change with the PA process but a reversible change without PA, which is consistent with the XRD results. Meanwhile, the $P_3$ intensity exhibits a significant enhancement after PA treatment. Such behavior confirms that Cu cations move further away from the center of $S_6$ octahedron (36). Furthermore, the $P_2$ and $P_4$ modes, which correspond to the $[P_2S_6]$ framework (35), also exhibit irreversible shifts after the pressure treatment with the PA process. A more detailed discussion on the structural variations can be found in *SI Appendix* (Page 2). These findings provide additional evidence for the retained structural changes induced by PA treatment. During the PA process, the high-pressure conditions cause the Cu cations to undergo structural rearrangements and reach a new equilibrium state with time. Subsequently, when the pressure is released, the Cu cations partially retain their new positions, leading to a permanent modification of the atomic structure. This structural change, particularly in the Cu configuration, has a direct impact on the electronic and physical properties of $CuInP_2S_6$, resulting in the retained enhancement of its ferroelectric and SHG performance.

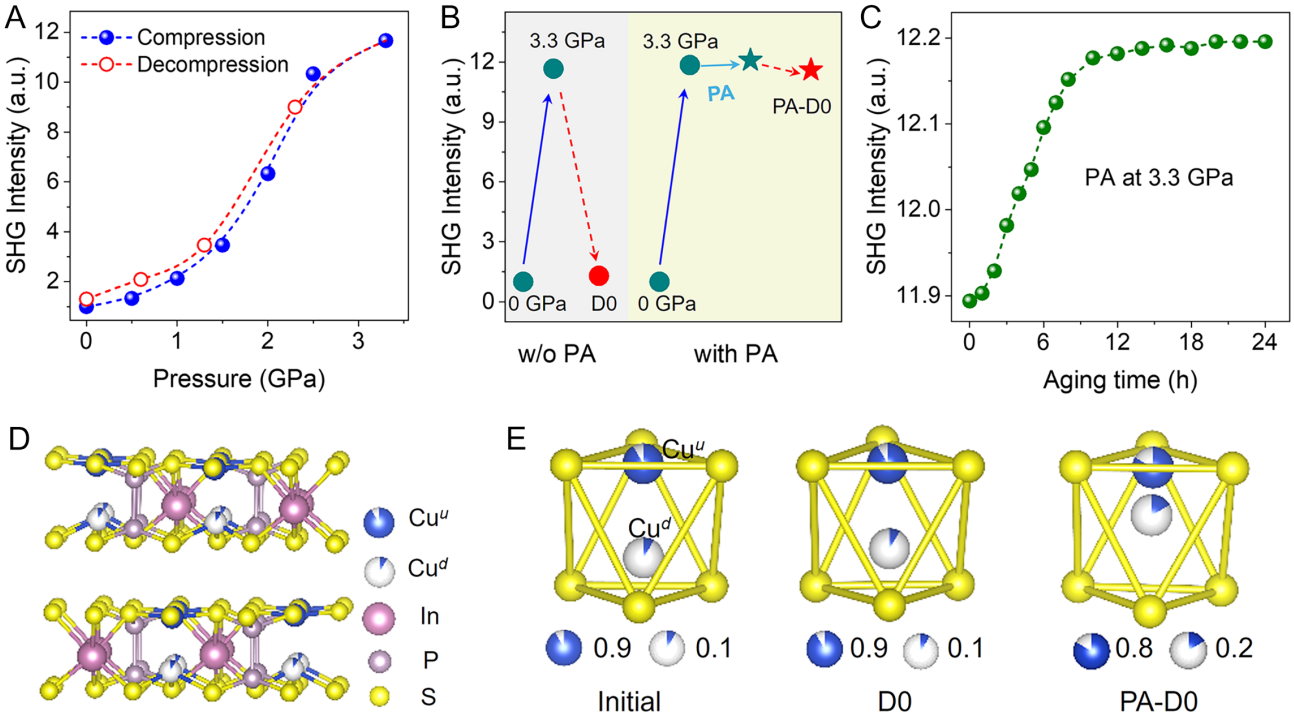


**Fig. 2.** The variations of SHG property and structure of $CuInP_2S_6$ during pressure treatments with and without PA. (*A*) Pressure-dependent SHG intensity of $CuInP_2S_6$, which shows reversible evolution throughout the compression and decompression cycle without the PA process. (*B*) Comparative analysis of the distinct variations of SHG during compression and decompression with and without PA. The pressure-induced enhancement of 12 times in SHG can be maintained for the sample that underwent PA treatment (PA-D0). In contrast, the sample without PA process exhibits a reversible variation during compression–decompression cycle (D0). (*C*) The time-dependent evolution of SHG intensities during the PA treatment at 3.3 GPa, which exhibits a continuous increase of SHG and eventually reaches a plateau over a period of 12 h. (*D*) The crystal structures of $CuInP_2S_6$ at initial conditions. (*E*) Comparative analysis of the variations of $Cu^u/Cu^d$ ratio and position at the initial state, after the pressure treatment with and without the PA process.

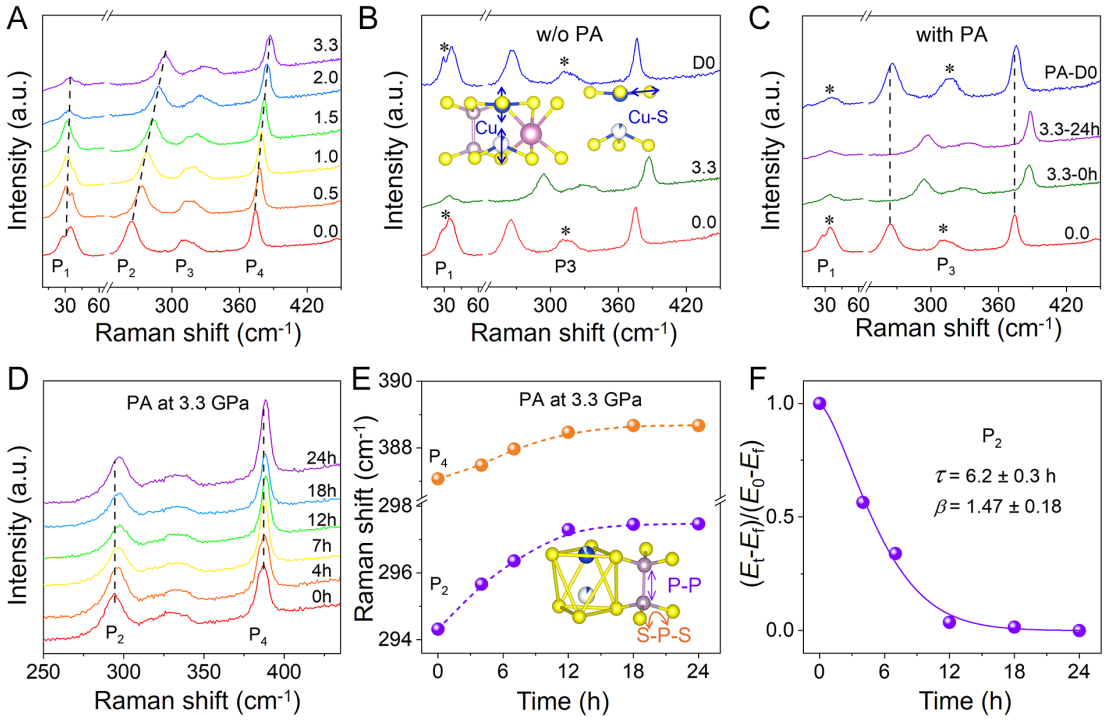


**Fig. 3.** Raman analysis of $CuInP_2S_6$ and the fundamental mechanism underlying the PA processes. (*A*) In situ Raman spectra of $CuInP_2S_6$ at selected pressures. The $P_1$ mode is identified as the out-of-plane vibration of Cu, and the weakening of its intensity confirms the increase in dispersion of Cu cations. $P_3$ mode is identified as the asymmetric stretching vibration of Cu–S. $P_2$ and $P_4$ modes correspond to the $[P_2S_6]$ framework. (*B* and *C*) The reversible and irreversible variations of Raman modes corresponding to both Cu configuration ($P_1$ and $P_3$, marked by asterisk) and $[P_2S_6]$ framework ($P_2$ and $P_4$, marked by dash line) without and with PA treatment. (*D*) The Raman spectra of $CuInP_2S_6$ at selected times during PA treatment at 3.3 GPa. (*E*) Time dependence of Raman peaks corresponding to the $[P_2S_6]$ framework (i.e., $P_2$ and $P_4$ modes). (*F*) The fitting of Raman energy variations during PA process using the Kohlrausch–Williams–Watts (KWW) relaxation function.

**Fundamental Mechanism Underlying the PA Process.** Further investigation is necessary to gain an understanding of the detailed mechanisms underlying the structural changes and property variations during the PA process. As mentioned earlier, the SHG intensity of $CuInP_2S_6$ continued to increase during PA at 3.3 GPa, eventually reaching a plateau over a period of 12 h (Fig. 2*C*). Concurrently, certain Raman peaks exhibited a progressive blue shift and also reached a plateau over the same 12-h duration (Fig. 3 *D* and *E*). These observations suggest a correlation between the continuous increase in SHG intensity and the blue shift of Raman peaks during the PA process, which experienced the same dynamic evolution. The PA treatment drives the material toward a new equilibrium state, resulting in the observed changes in structures and properties over time.

In-depth analyses are required to elucidate the relaxation dynamics and establish a comprehensive understanding of the temporal evolution of these changes during the PA process. Notably, as shown in Fig. 3*F* and *SI Appendix*, Figs. S11 and S12, the relaxation processes for both structure (Raman) and property (SHG) can be expressed using the Kohlrausch–Williams–Watts (KWW) function (37–39), $F(t) = F_0\exp[-(t/\tau)^{\beta}]$, where $F(t)$ represents the difference between the observed quantity at the time $t$ and value at the final timepoint, $F_0$ is the difference between the observed quantity at the initial and final states, $\tau$ is the relaxation time, and $\beta$ denotes the PA exponent. The KWW function effectively captures the intricate time-dependent dynamic processes, allowing for a precise fitting of physical parameters related to both structure (Raman shift) and property (SHG intensity). Specifically, by fitting the shift of Raman peaks and the variation of SHG intensity using the KWW relaxation function, the relaxation time $\tau$ is derived to be around 6 h, and the PA exponent $\beta$ is determined to be around 1.5 which aligns with previously reported $\beta$ values observed in the relatively soft materials (40–42). In the case of $CuInP_2S_6$, an aging period of over 6 h is required to achieve a permanent and substantial enhancement in its property. This is attributed to the fact that the PA relaxation process involves different response rates for various components of the materials to the applied pressure. This necessitates a relatively prolonged duration to reach a new equilibrium state. Specifically, a 1-h PA treatment yielded a negligible change, and a 3-h treatment led to slight property enhancement (*SI Appendix*, Fig. S13). In contrast, the 6- and 12-h PA treatments resulted in a pronounced enhancement. In addition, the PA relaxation dynamics can be facilitated at higher temperatures. As shown in *SI Appendix*, Fig. S14, the $\tau$ value decreases to 4.4 h and 3.2 h with temperature increasing to 35 °C and 55 °C, respectively.

**General Applicability of PA Strategy for a Broad Class of Materials.** Furthermore, the applicability and significance of the PA strategy have been demonstrated with diverse materials possessing different structural characteristics, including 3D perovskite $MHyPbBr_3$ (MHy = $CH_3NH_2NH_2$), 2D perovskite $(BA)_2(GA)Pb_2I_7$ [BA = $CH_3CH_2CH_2CH_2NH_2$, GA = $C(NH_2)_3$], 1D $(CH_3CH_2CH_2NH_3)_2SbBr_5$, 0D $(MePh_3P)_2SbCl_5$ ($MePh_3P$ = $CH_3(C_6H_5)_3P$), etc., as summarized in Fig. 4*a*. In all these systems, the application of PA treatment leads to permanent structural modifications and properties improvements after pressure release, while reversible variations are observed without the PA process. Specifically, the 3D $MHyPbBr_3$ exhibits a tenfold increase in SHG intensity after PA at 1.5 GPa for 24 h (*SI Appendix*, Fig. S15); the 2D $(BA)_2(GA)Pb_2I_7$ demonstrates a twofold increase in PL intensity (*SI Appendix*, Fig. S16); the 1D $(CH_3CH_2CH_2NH_3)_2SbBr_5$ exhibits an emerging and strong SHG that is negligible without PA (*SI Appendix*, Fig. S17); the 0D $(MePh_3P)_2SbCl_5$ shows a notable rise in recombination rate $k$ following the PA treatment (*SI Appendix*, Fig. S18).

This PA strategy, emphasizing the importance of the duration spent at the desired pressures, distinguishes it from the previous

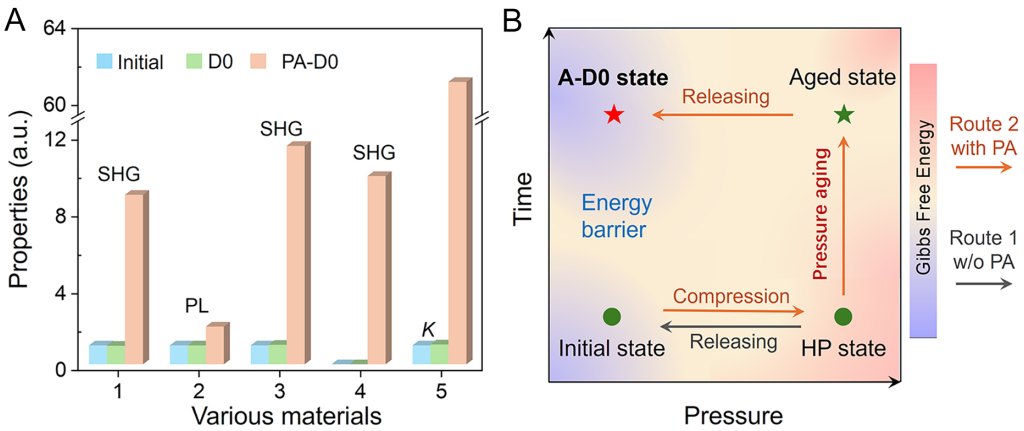


**Fig. 4.** The applicability of PA strategy for various materials. (*A*) The implementation of PA strategy leads to significant improvements in the properties of diverse materials. The designations 1 to 5 correspond to the materials of 3D $MHyPbBr_3$, 2D $(BA)_2(GA)Pb_2I_7$, 2D $CuInP_2S_6$, 1D $(CH_3CH_2CH_2NH_3)_2SbBr_5$, and 0D $(MePh_3P)_2SbCl_5$, respectively. (*B*) The illustration of potential mechanism for the PA recovery process.

efforts that focus primarily on the applied pressure values. For instance, Xiao et al. have reported the synthesis of several nanomaterials, including CdSe nanowires and Au hetero-rods, achieved through pressure-induced consolidation or fusion at around 15 GPa (11, 43–45); Yang et al. have realized the high performance of isophthalic acid and $Zn_4O(ADC)_4(Et_3N)_6$ MOF nanocrystals (ADC = acetylenedicarboxylic, $Et_3N$ = triethylamine) at around 20 GPa by pressure-enhanced hydrogen bonding and pressure-modulated carbonyls aggregation, respectively (46, 47); Gao et al. have reported the pressure-induced polymerization of molecules containing unsaturated chemical bonds at approximately 20 GPa (48, 49). In these cases, the pressure-induced fusion of nanomaterials or chemical reactions exists where the pressure value dominates. In our case, experimental results have demonstrated the broad applicability of the PA process for exploring and stabilizing a wide range of exceptional high-pressure materials. Particularly, by integrating the temporal aspect, materials harboring multiple metastable phases accessible through the PA treatment are amenable to such recovery approach. The potential mechanism of such phenomena is illustrated in Fig. 4*B*. The PA-induced changes in local interactions, such as hydrogen bonding and steric hindrance, are believed to play a crucial role in locking in these metastable phases, enabling the durable preservation of their desirable properties even after the release of applied pressure. The versatility of the PA strategy across different structural dimensionalities and material systems highlights its transformative potential in unlocking the practical applications of high-pressure-derived functional materials.

## Conclusion and Outlook

In summary, we have proposed a previously undescribed concept of pressure aging that has demonstrated its significance and general applicability across a wide variety of materials. The PA approach is capable of inducing permanent structural modifications and property improvements that persist even after pressure is released and the material returns to ambient conditions. This sets it apart from reversible variations that are typically observed during high-pressure treatment without the PA process. As a demonstrative example, 2D ferroelectric $CuInP_2S_6$ exhibits a permanent change in Cu configuration and brings a significant property improvement through PA treatment at 3.3 GPa for 24 h. Its remanent polarization increased by 2.5 times and its $T_c$ rises from 317 K to 583 K after the pressure is fully released. In contrast, reversible variations are observed for the sample subjected to the compression–decompression cycle but without the 24-h PA process. The broad applicability of PA strategy has been demonstrated with various materials such as 3D halide perovskite $MHyPbBr_3$, 2D $(BA)_2(GA)Pb_2I_7$, 1D $(CH_3CH_2CH_2NH_3)_2SbBr_5$, and 0D $(MePh_3P)_2SbCl_5$. The relaxation dynamics during the PA process have been elucidated through the fitting of the Kohlrausch–Williams–Watts function, revealing a shared dynamic mechanism across different materials. The implementation of PA concept introduces a unique dimension to high-pressure research field, broadening the horizons for the exploration of novel materials with optimized structures and enhanced functionalities. Notably, the pressures involved are industrially attainable, and the sample size can be scaled up for innovative applications and technological advancements.

## Materials and Methods

**$CuInP_2S_6$.** Copper powder (Aladdin, 99.9%), indium powder (Aladdin, 99.99%), red phosphorus lump (Aladdin, 98.5%), and sulfur powder (Aladdin, 99.95%) were weighed in accordance with a stoichiometric ratio of 1:1:2:6. The raw materials were put together and sealed in a fused quartz tube under high vacuum ($\sim 10^{-3}$ Pa). The tube was then heated to 600 °C over 12 h and soaked for 10 d in a muffle furnace to fabricate polycrystalline $CuInP_2S_6$ bulk. High-quality $CuInP_2S_6$ single-crystal flakes were fabricated by the chemical vapor transport method. The as-synthesized polycrystalline bulk (3 g) and transport agent $I_2$ (50 mg) were put at the bottom of a tube. The tube was sealed as before, placed, and heated in a two-zone furnace with 680 and 750 °C for 7 d. The bottom of the tube was placed in the hot zone. After the transport process, yellow crystals were obtained in the cold zone.

**$MHyPbBr_3$.** Single-crystal $MHyPbBr_3$ (MHy = $CH_3NH_2NH_2$) was grown using an antisolvent method. Precursor solution was obtained by dissolving $PbBr_2$ (1.835 g, 5 mmol) and methylhydrazine sulfate (0.721 g, 5 mmol) in an aqueous HBr solution (48%, 4 mL) under stirring. Then, 1 mL of the precursor solution was placed into a glass vial, which was then placed in a larger vial containing methanol. The lid of the outer vial was sealed, while the lid of the inner vial was completely open, allowing the diffusion of methanol into the precursor solution. Yellow crystals formed within one day.

**$(BA)_2(GA)Pb_2I_7$.** For synthesizing $(BA)_2(GA)Pb_2I_7$ [BA = $CH_3CH_2CH_2CH_2NH_2$, GA = $C(NH_2)_3$], 5.71 mmol $PbI_2$ and 2.86 mmol guanidine hydrochloride was dissolved in 9 mL HI solution and 1 mL of $H_3PO_2$ in a vial. Then, 2.86 mmol butylamine was added into the solution, and all reagents were dissolved under heating and stirring. Then, heating was stopped and red single crystals precipitated during cooling.

**$(CH_3CH_2CH_2NH_3)_2SbBr_5$.** The prototype of 1D lead-free perovskite $(CH_3CH_2CH_2NH_3)_2SbBr_5$ was prepared by combining antimony trioxide (291.5 mg, 1 mmol) and n-propylamine (236.44 mg, 4 mmol) in 5 mL of hydrobromic acid. Then, the mixture was heat and stirred briskly until dissolved. Subsequently, slowly cooling the solution to room temperature yielded yellow needlelike crystals.

**$(MePh_3P)_2SbCl_5$.** First, 0.63 mmol $SbCl_3$ (143.6 mg) and 1.26 mmol $MePh_3PCl$ [$MePh_3P = CH_3(C_6H_5)_3P$] (395.4 mg) were mixed at 1:2 molar ratio and dissolved in 6 mL DMF to form a clear precursor solution. Bulk crystals were obtained by diffusing 2 mL $Et_2O$ into 1 mL DMF solution at room temperature overnight. The large colorless crystals were washed with $Et_2O$ and dried under reduced pressure. Yield: 85%.

**Pressure Control Devices.**

***Diamond anvil cells.*** The high-pressure measurement environment was provided by symmetrical diamond anvil cells (DACs). Ultralow fluorescence diamonds with a culet size of 400 μm were used. The high-pressure sample chamber was formed from a preindented T301 stainless steel gasket with a thickness of about 50 μm and a hole with a diameter of about 250 μm by laser-drilling the center part of it. The sample and a ruby ball (for pressure measurements) were loaded inside the chamber, and the pressures were determined by the ruby fluorescence method. Silicon oil was used as the pressure-transmitting medium.

***High-pressure torsion system.*** The large sample utilized the TRANSMST HPT-T6 high-pressure torsion system, with the accompanying anvils made of high-strength steel. We selected an appropriate anvil model and ensured its surface is thoroughly polished and then set the target pressure and initiate the program. A semiconstrained anvil with a groove size of 10 mm in diameter and 0.25 mm in depth is employed. A steel gasket with a hole size of 7 mm drilled in the center was used to place the sample. Silicone grease was used as a pressure transmission medium.

***The voltage- and frequency-dependent P–E loops.*** Frequency- and voltage-dependent P–E hysteresis loops of CuInP2S6 were measured by the aix-ACCT System TF 1000 in the Dynamic hysteresis measurement (DHM) mode. The DHM records the hysteresis loop of a ferroelectric material and assists to examine the influence of process parameters on the shape of the hysteresis loop. Measurement parameters like amplitude or frequency of the excitation signal can be varied. The software extracts the characteristic values like P, V, etc. from the hysteresis loop.

***SHG measurement.*** SHG experiments were measured using a home-built system. A femtosecond laser (NPI LASER Co., Ltd., 1030 nm, 25 MHz, 200 fs. The peak power and energy-per-pulse of laser for SHG is 0.5 mW and 1 × 10−12 J was used as the exciting light source. A 20× objective was used to focus the laser with a beam size of 4 μm in diameter. A spectrometer (Nova, Ideaoptics Co., Ltd.) was employed to collect the SHG signal. The polarization-dependent SHG experiment was carried out by linearly polarized light. The generation of the linear polarization was based on rotating a half-wave plate. The linearly polarized light focused on the surface of a high-quality single crystal, and the subsequently excited SHG signal was detected by the spectrometer. The temperature-dependent SHG measurements were conducted using a microscope cryostat system (Janis ST-500).

***Photoluminescence (PL) spectroscopy.*** The PL spectra were collected using a home-designed spectroscopy system (Gora-UVN-FL, assembled by Ideaoptics, Shanghai, China). PL spectra were measured using a 360 nm excitation laser at a power of 10 μW.

***Time-resolved PL spectroscopy.*** Time-resolved PL measurements were performed using the time-correlated single-photon counting (TCSPC) electronics PicoHarp300 of the PicoQuant FluoTime 300 (PicoQuant GmbH, Germany), equipped with a PDL 820 laser pulse driver. A pulsed laser diode LDH-P-C-405 (λex = 405 nm, pulse FWHM = 20 nm, repetition rate 30 kHz and 20 MHz. The peak power for time-resolved photoluminescence is 10 and 20 mW. The energy-per-pulse of time-resolved photoluminescence is 2.2 × 10−13 and 3.3 × 10−13 J was used to excite the sample. The photons were collected by a PMA-C-192 photomultiplier (PMT) single-photon-counting detector. The data were acquired and analyzed by using commercially available software EasyTau (PicoQuant GmbH, Germany).

***Raman spectroscopy.*** Raman spectra were collected using a home-built low-wavenumber Raman system (532 nm for CuInP2S6). The Raman signal was collected by a spectrograph (IsoPlane 320, Princeton Instruments) coupled to a nitrogen-cooled detector (PyLon100BR_eXcelon, Princeton Instrument).

***X-ray diffraction (XRD) crystallography.*** Single-crystal XRD measurements were conducted on a Bruker D8 Venture diffractometer utilizing Mo $K_\alpha$ radiation. The crystal structures of the samples were solved and refined using APEX3 software.

**Data, Materials, and Software Availability.** All study data are included in the article and/or *SI Appendix*.

**ACKNOWLEDGMENTS.** This work is supported by the National Nature Science Foundation of China (NSFC) (Grant Nos. 22275004, U1930401, 42150101, and 52073155), Shanghai Key Laboratory of Novel Extreme Condition Materials (No. 22dz2260800), and Shanghai Science and Technology Committee (No. 22JC1410300). Some experiments are supported by the Synergetic Extreme Condition User Facility (SECUF).

Author affiliations: [a]Center for High Pressure Science and Technology Advanced Research, Shanghai 201203, China; [b]State Key Laboratory of New Ceramics and Fine Processing, School of Materials Science and Engineering, Tsinghua University, Beijing 100084, China; [c]State Key Laboratory of Molecular Reaction Dynamics and Dynamics Research Center for Energy and Environmental Materials, Dalian Institute of Chemical Physics, Chinese Academy of Sciences, Dalian, Liaoning 116023, China; [d]Shanghai Key Laboratory MFree, Institute for Shanghai Advanced Research in Physical Sciences, Shanghai 201203, China; and [e]Beijing National Laboratory for Molecular Science, College of Chemistry and Molecular Engineering, Peking University, Beijing 100871, China

1. P. F. McMillan, New materials from high-pressure experiments. *Nat. Mater.* **1**, 19–25 (2002).
2. L. Zhang, Y. Wang, J. Lv, Y. Ma, Materials discovery at high pressures. *Nat. Rev. Mater.* **2**, 1–16 (2017).
3. H. K. Mao, X. Chen, Y. Ding, B. Li, L. Wang, Solids, liquids, and gases under high pressure. *Rev. Mod. Phys.* **90**, 015007 (2018).
4. M. Miao, Y. Sun, E. Zurek, H. Lin, Chemistry under high pressure. *Nat. Rev. Chem.* **4**, 508–527 (2020).
5. M. Santoro *et al.*, Amorphous silica-like carbon dioxide. *Nature* **441**, 857–860 (2006).
6. Q. Huang *et al.*, Nanotwinned diamond with unprecedented hardness and stability. *Nature* **510**, 250–253 (2014).
7. Q. Hu *et al.*, $FeO_2$ and FeOOH under deep lower-mantle conditions and Earth's oxygen–hydrogen cycles. *Nature* **534**, 241–244 (2016).
8. Y. Yue *et al.*, Hierarchically structured diamond composite with exceptional toughness. *Nature* **582**, 370–374 (2020).
9. H. Tang *et al.*, Synthesis of paracrystalline diamond. *Nature* **599**, 605–610 (2021).
10. Y. Shang *et al.*, Ultrahard bulk amorphous carbon from collapsed fullerene. *Nature* **599**, 599–604 (2021).
11. T. Xiao *et al.*, Nanocrystals with metastable high-pressure phases under ambient conditions. *Science* **377**, 870–874 (2022).
12. K. Bu *et al.*, Nested order-disorder framework containing a crystalline matrix with self-filled amorphous-like innards. *Nat. Commun.* **13**, 4650 (2022).
13. W. L. Mao, Y. Lin, Making the most of metastability. *Science* **377**, 814–815 (2022).
14. Y. Wu *et al.*, Twisted-layer boron nitride ceramic with high deformability and strength. *Nature* **626**, 779–784 (2024).
15. M. I. Eremets, R. J. Hemley, H. K. Mao, E. Gregoryanz, Semiconducting non-molecular nitrogen up to 240 GPa and its low-pressure stability. *Nature* **411**, 170–174 (2001).
16. A. Drozdov, M. Eremets, I. Troyan, V. Ksenofontov, S. I. Shylin, Conventional superconductivity at 203 kelvins at high pressures in the sulfur hydride system. *Nature* **525**, 73–76 (2015).
17. F. Bai, K. Bian, X. Huang, Z. Wang, H. Fan, Pressure induced nanoparticle phase behavior, property, and applications. *Chem. Rev.* **119**, 7673–7717 (2019).
18. V. Minkov, V. Ksenofontov, S. Bud'ko, E. Talantsev, M. Eremets, Magnetic flux trapping in hydrogen-rich high-temperature superconductors. *Nat. Phys.* **19**, 1293–1300 (2023).
19. H. Luo *et al.*, Anomalous charge transfer from organic ligands to metal halides in zero-dimensional $[(C_6H_5)_4P]_2SbCl_5$ enabled by pressure-induced lone pair-π interaction. *Angew. Chem. Int. Ed.* **62**, e202304494 (2023).
20. P. Bhattacharyya *et al.*, Imaging the Meissner effect in hydride superconductors using quantum sensors. *Nature* **627**, 73–79 (2024).
21. S. Guo *et al.*, Exciton engineering of 2D Ruddlesden–Popper perovskites by synergistically tuning the intra and interlayer structures. *Nat. Commun.* **15**, 3001 (2024).
22. R. Hemley, H. K. Mao, *Overview of Static High Pressure Science* (IOS Press, 2002), pp. 3–40.
23. S. V. Sinogeikin *et al.*, Online remote control systems for static and dynamic compression and decompression using diamond anvil cells. *Rev. Sci. Instrum.* **86**, 072209 (2015).
24. P. Verleysen, H. Lanjewar, Dynamic high pressure torsion: A novel technique for dynamic severe plastic deformation. *J. Mater. Process. Tech.* **276**, 116393 (2020).
25. L. Xu, S. Liu, Y. Cheng, H. Qian, Nutrition., The effect of aging on beef taste, aroma and texture, and the role of microorganisms: A review. *Crit. Rev. Food Sci.* **63**, 2129–2140 (2023).
26. Y. He *et al.*, Research progress of wine aroma components: A critical review. *Food Chem.* **402**, 134491 (2023).
27. R. Bian *et al.*, Recent progress in the synthesis of novel two-dimensional van der Waals materials. *Natl. Sci. Rev.* **9**, nwab164 (2022).
28. V. Maisonneuve, V. Cajipe, A. Simon, Von Der Muhll, J. R. Ravez, Ferrielectric ordering in lamellar $CuInP_2S_6$. *Phys. Rev. B* **56**, 10860 (1997).

29. J. A. Brehm *et al.*, Tunable quadruple-well ferroelectric van der Waals crystals. *Nat. Mater.* **19**, 43–48 (2020).
30. K. Bu *et al.*, Enhanced second-harmonic generation of van der Waals $CuInP_2S_6$ via pressure-regulated cationic displacement. *Chem. Mater.* **35**, 242–250 (2022).
31. X. Yao *et al.*, Anomalous polarization enhancement in a van der Waals ferroelectric material under pressure. *Nat. Commun.* **14**, 4301 (2023).
32. D. Rong *et al.*, Ion migration induced bipolar diode effect and ferroelectricity modulation in $CuInP_2S_6$. *Appl. Phys. Lett.* **122**, 181902 (2023).
33. Z. Zhou *et al.*, Sliding-mediated ferroelectric phase transition in $CuInP_2S_6$ under pressure. *Appl. Phys. Rev.* **11**, 011414 (2024).
34. L. You *et al.*, Origin of giant negative piezoelectricity in a layered van der Waals ferroelectric. *Sci. Adv.* **5**, eaav3780 (2019).
35. Y. M. Vysochanskii, V. Stephanovich, A. Molnar, V. Cajipe, X. Bourdon, Raman spectroscopy study of the ferrielectric-paraelectric transition in layered $CuInP_2S_6$. *Phys. Rev. B* **58**, 9119 (1998).
36. S. N. Neal *et al.*, Vibrational properties of $CuInP_2S_6$ across the ferroelectric transition. *Phys. Rev. B* **105**, 075151 (2022).
37. G. Williams, D. C. Watts, Non-symmetrical dielectric relaxation behaviour arising from a simple empirical decay function. *Trans. Faraday Soc.* **66**, 80–85 (1970).
38. B. Ruta *et al.*, Atomic-scale relaxation dynamics and aging in a metallic glass probed by x-ray photon correlation spectroscopy. *Phys. Rev. Lett.* **109**, 165701 (2012).
39. N. Rabiei, S. H. Amirshahi, M. Haghighat Kish, Description of physical aging kinetics of glassy polymers by interpretation of parameters of the Kohlrausch-Williams-Watts relaxation function via simulation. *Phys. Rev. E* **99**, 032502 (2019).
40. L. Cipellett, S. Manley, R. C. Ball, D. A. Weitz, Universal aging features in the restructuring of fractal colloidal gels. *Phys. Rev. Lett.* **84**, 2275–2278 (2000).
41. L. Cipelletti *et al.*, Universal non-diffusive slow dynamics in aging soft matter. *Faraday Discuss.* **123**, 237–251 (2003).
42. R. Bandyopadhyay *et al.*, Evolution of particle-scale dynamics in an aging clay suspension. *Phys. Rev. Lett.* **93**, 228302 (2004).
43. B. Li *et al.*, Pressure compression of CdSe nanoparticles into luminescent nanowires. *Sci. Adv.* **3**, e1602916 (2017).
44. H. Zhu *et al.*, Pressure-enabled synthesis of hetero-dimers and hetero-rods through intraparticle coalescence and interparticle fusion of quantum-dot-Au satellite nanocrystals. *J. Am. Chem. Soc.* **139**, 8408–8411 (2017).
45. R. Li, J. Zhu, B. Ge, Z. Wang, Pressure-driven interplay between soft and hard components and resultant anisotropic and topological responses in a Pt nanocube assembled rhombohedral superlattice. *Chem. Mater.* **35**, 9412–9422 (2023).
46. Q. Yang *et al.*, Brightening triplet excitons enable high-performance white-light emission in organic small molecules via integrating n-$\pi^*$/$\pi$-$\pi^*$ transitions. *Nat. Commun.* **15**, 7778 (2024).
47. Z. Xiao *et al.*, Harvesting multicolor photoluminescence in nonaromatic interpenetrated metal-organic framework nanocrystals via pressure-modulated carbonyls aggregation. *Adv. Mater.* **36**, e2403281 (2024).
48. D. Gao *et al.*, Crystalline $C_3N_3H_3$ tube (3,0) nanothreads. *Proc. Natl. Acad. Sci. U.S.A.* **119**, e2201165119 (2022).
49. P. Zhang *et al.*, Ordered Van der Waals hetero-nanoribbon from pressure-induced topochemical polymerization of azobenzene. *J. Am. Chem. Soc.* **145**, 6845–6852 (2023).